Two-Scale Sparse Spiral Array Design for 3D Ultrasound Imaging in Air

**GIANNI ALLEVATO[ID], CHRISTOPH HAUGWITZ[ID] (Student Member, IEEE),
MATTHIAS RUTSCH, RAPHAEL MÜLLER[ID], MARIUS PESAVENTO[ID] (Senior Member, IEEE),
AND MARIO KUPNIK[ID] (Senior Member, IEEE)**

Department of Electrical Engineering and Information Technology, Technische Universität Darmstadt, 64283 Darmstadt, Germany

CORRESPONDING AUTHOR: G. ALLEVATO (gianni.allevato@tu-darmstadt.de)

ABSTRACT Sparse array designs are a promising approach to improve the beam pattern and imaging quality, especially for applications, where hardware resources are severely limited. In particular, spiral sunflower arrays become increasingly popular due to their excellent point-spread-function (PSF) characteristics and their simple, deterministic and scalable design. Therefore, several sunflower modifications for further improvement have been investigated, e.g. density tapering based on window functions adapted from apodization techniques. In this article, we introduce a two-scale spiral array design concept, which exploits the specific PSF structure of the sunflower geometry, instead of relying on window functions. The modification proposed combines two nested sunflower sub-arrays featuring two different spatial element densities such that the locations of their respective main, side and grating lobe zones differ, resulting in a balanced and improved composite one-way PSF in terms of main lobe width (MLW) and maximum side lobe level (MSLL) under far-field and narrow-band conditions. First, we provide an analysis of the unmodified classic sunflower geometry, describe its PSF zones and show how their locations in the PSF can be estimated based on the array design parameters, which finally leads to the two-scale concept. Second, we examine a specific well-matching combination of nested sub-arrays to discuss the advantages and limitations of the resulting PSF. Third, we benchmark the respective optimum arrays of the classic sunflower and density tapering strategies with the two-scale method, where the latter shows an improved performance of the one-way PSF in terms of MLW and MSLL. Fourth, the two-scale design strategy is validated using a real-world 64-element prototype for narrow-band ultrasound imaging in air. We conduct two experiments to analyze the resulting PSF and angular resolution. Overall, the results demonstrate that the proposed flexible four-parameter concept is particularly valuable for high frame rate imaging as well as for transmit-only and receive-only applications.

INDEX TERMS Sparse array, spiral array, phased array, ultrasound, sonar, imaging.

I. INTRODUCTION

ONE of the major challenges of ultrasonic 3D imaging systems, as used for non-destructive testing, environmental perception and medical diagnostics, is to maintain image contrast while ensuring a high angular resolution and fast volume rates. Bringing these competing requirements together is particularly difficult for emerging application fields, where mobility is crucial and hardware resources are severely limited. These advancing technologies range from sonar systems, which provide a complementary perception sensor modality for upcoming mobile autonomous robotics [1], [2], [3], up to portable medical point-of-care scanners, which enable life-saving diagnoses outside the hospital, e.g. directly at the scene of an accident or for medics in combat [4], [5], [6].

In both application examples, the 3D images are generated using beamforming, so that contrast and angular resolution are typically quantified based on the maximum secondary lobe level (MSLL) and the main lobe width (MLW) obtained from the point spread function (PSF). The PSF itself is dependent on the beamforming technique and the array geometry employed, both of which provide a respective computational and physical starting point for improvement, where the latter is the focus of this article.

In order to realize and enhance volumetric high-frame-rate imaging on hardware-limited devices, a promising approach

is to combine low-complexity conventional beamforming with sparse array designs. Unlike traditional fully-populated arrays, the aperiodic element positioning of sparse arrays prevents severe MSLL degradation due to high grating lobes even if the inter-element spacings exceed half wavelength ($\lambda/2$) [7]. This way, large-aperture 2D arrays can be created for improving the MLW without requiring a drastic increase in the number of elements, system complexity and cost.

Sparse array synthesis is grouped into two categories, i.e. stochastic and deterministic designs [8], [9]. Stochastic sparse arrays rely on a randomized element positioning paired with optimization schemes, e.g. genetic algorithms [10], [11], [12], [13] or simulated annealing [14], [15], [16], [17], in order to optimize for pre-defined quality metrics. In contrast, deterministic methods provide a parametric approach, that is easily controllable and scalable, allowing a rapid and flexible customization to satisfy application constraints [18], [19], [20], [21]. Additionally, the resulting geometry can be used as a seed for a further optimization procedure as it already features decent characteristics from the start.

A specific deterministic sparse array design is based on the Fermat spiral. In particular, the sunflower pattern [22], which results from sampling the Fermat spiral with Golden-Angle increments, is highly effective at suppressing grating lobes due to the aperiodic unique element positioning with approximately uniform spatial density [23]. These sparse spiral arrays become increasingly popular in multiple areas, such as satellite communications [24], [25], antenna arrays for radar imaging and 5G communication [26], [27], [28], [29], optical phased arrays [30], [31], [32], [33], acoustic noise localization [34], [35], [36] and many ultrasound applications. The latter field includes air-coupled array technologies, e.g. for haptic feedback [37], highly directive proximity sensing in agriculture [38], [39], and in-air imaging [40], [41], [42], as well as medical ultrasound applications, such as high-intensity focused ultrasound (HIFU) [43], [44], [45], [46] and diagnostic imaging [47], [48], [49], [50], [51], [52], [53], [54], [55]. In order to further improve the characteristics of the spiral sunflower array, multiple modifications have been proposed.

In [56], the authors presented a spiral sunflower design modification based on two-way line-by-line beamforming, where the transmit and receive array geometries differ. By excluding specific adjacent spiral arms in the transmit and receive array pairs, the positions of the secondary lobe maxima and minima in the respective PSFs can be manipulated such that they cancel out. Although this method can effectively reduce the overall side lobe level, relying on two-way line-by-line beamforming is impractical for volumetric imaging applications that require a minimum number of firing events to achieve high frame rates. Therefore, we focus on concepts for improving the one-way PSF characteristics, which are also valuable for transmit- or receive-only applications apart from imaging.

A method for improving the general one-way PSF by modifying the spiral sunflower array geometry, referred to as density tapering, has been proposed for antenna arrays in [25]. Density tapering adapts the idea of weighting the element sensitivities based on a spatial window function to reduce the side lobe level, also known as apodization [57]. However, instead of weighting the sensitivities themselves, the spatial density of the element distribution is altered depending on the window function. This way, the MLW and MSLL can be fine-tuned without sacrificing overall sensitivity. In [48], density tapered spiral arrays have been examined for ultrasound imaging including a comparison of multiple window functions. Additionally, the authors have created two 256-element CMUT and PZT array prototypes [58], [59], [60] based on a Blackman window taper and experimentally evaluated various medical ultrasound imaging applications [49], [50], [51], [52], [53]. In [61], Sarradj investigated another density tapering approach based on a parametric window function and a non-linear least squares method for element positioning, enabling a flexible one-parameter control of the taper.

In this article, we introduce a two-scale sparse spiral array design concept, which exploits the specific PSF structure of sunflower arrays, instead of relying on window functions for density tapering. The modification proposed combines two nested sunflower sub-arrays featuring two different spatial element densities such that the locations of their respective main lobe, side lobes and grating lobes, referred to as PSF zones, differ and combine favorably. As a result, the composite array geometry has a balanced and improved one-way narrow-band PSF in the far-field in terms of MSLL and MLW compared to the previous approaches.

The main contributions are grouped into four categories. First, we provide an analysis of the PSF characteristics of the unmodified classic sunflower array for different aperture diameters and number of elements in order to introduce a concept for estimating the PSF zone locations requiring only the basic array design parameters. Second, we elaborate the two-scale array design and extend the PSF zone estimation for its sub-arrays. In addition, we investigate a specific well-matching sub-array combination for highlighting its advantages and limitations. Third, we benchmark the respective 64-element and 256-element arrays of the classic sunflower and density tapering strategies with the two-scale method and examine multiple optimum sub-array combinations in more detail. Fourth, the two-scale design strategy is validated using a real-world prototype for ultrasound imaging in air, which consists of 64 MEMS microphones and one piezoelectric ultrasonic transducer. Based on this prototype, we conduct two experiments to analyze the resulting PSF and angular resolution.

The remainder of this article is organized as follows. Section II includes the model for generating the beam patterns and PSF, as well as the analysis of the classic sunflower geometry and its PSF zone estimation. Based on this, the two-scale array design is introduced along with the evaluation

of a well-matching sub-array combination. Section III covers the benchmarking and the optimum two-scale sub-array combinations. Section IV includes the real-world prototype and experiments for validation. Finally, we conclude and discuss further ideas for improvement, as well as remaining questions in Section V.

II. METHODS

Here, we describe the classic sunflower array geometry and analyze the resulting PSF behavior in terms of MLW and MSLL for variable aperture sizes and number of elements. In addition, we introduce the different PSF zones observed and methods to estimate their locations which finally lead to the two-scale array design concept.

A. BEAM PATTERN AND POINT SPREAD FUNCTION MODEL

The key factors for the following evaluations are the far-field beam pattern and one-way PSF, i.e. the beam pattern with a single centered point source. The model used for their generation is based on the normalized and discretized well-known Rayleigh integral, where we assume point elements and point sources, as well as far-field and narrow-band conditions. Therefore, the model allows an application-independent analysis focused on the array element positions, as the effects of a particular element size, focal distance, or specific bandwidth are not included. The superimposed magnitude p for the beam pattern scanning direction $(u, v) = (\sin(\theta)\cos(\varphi), \sin(\varphi))$ is given by

$$p(u, v) = \left| \mathbf{a}^H(u, v) \left(\sum_{l=0}^{L-1} \mathbf{a}(u_l, v_l) \cdot p_{el}(u_l, v_l) \cdot s_l \right) \right|, \quad (1)$$

where θ and φ are the azimuth and elevation angles, L is the number of point sources, l is the corresponding source index, (u_l, v_l) and s_l are the l-th source direction and magnitude, respectively, and $\mathbf{a}(u, v) \in \mathbb{C}^{M \times 1}$ is the array-specific steering vector, whose m-th entry is given by

$$\mathbf{a}_m(u, v) = \exp\left(j\frac{2\pi}{\lambda}(x_m u + y_m v) \right). \quad (2)$$

Here, M is the number of elements and (x_m, y_m) is the position of the m-th array element. The term $p_{el}(u_l, v_l)$ includes the directivity of the elements themselves and is negligible if point elements are assumed, i.e. $p_{el} = 1$. Otherwise, if elements with extended sizes are considered, p_{el} can be calculated by sampling the element aperture, as explained in [40], that is

$$p_{el}(u_l, v_l) = \frac{1}{K} \sum_{k=0}^{K-1} \exp\left(j\frac{2\pi}{\lambda}(x_k u_l + y_k v_l) \right), \quad (3)$$

where K is the number of sample points, k the sample point index and (x_k, y_k) is the sample point position. The PSF is generated by evaluating (1) for the directions in the complete hemisphere, i.e. $\sqrt{u^2 + v^2} \leq 1$ (if not stated otherwise), and for a single centered point source, such that $L = 1$, $s_l = 1$ and

$(u_l, v_l) = (0, 0)$. The beam patterns and PSFs are generally normalized to their maximum value.

B. CHARACTERISTICS OF THE CLASSIC SUNFLOWER SPIRAL ARRAY

The position of the m-th element of the planar classic sunflower array $\mathbf{r}_m$ is determined by discretely sampling the Fermat spiral based on the models in [22] and [61] with the design parameter $V = 5$, that is

$$(R_m, \phi_m) = \left(R_{ap}\sqrt{\frac{m}{M}}, \; 2\pi(m-1)\frac{1+\sqrt{V}}{2} \right), \text{ and } \quad (4)$$

$$\mathbf{r}_m = (x_m, y_m) = (R_m \cos(\phi_m), R_m \sin(\phi_m)), \quad (5)$$

where R_m is the corresponding radius of the m-th element to the aperture center, ϕ_m is the corresponding angle and $R_{ap} = D_{ap}/2$ is the maximum aperture radius. The model defines the element radii to the center R_m such that the area of the ring spanned by two successive radii is constant and equivalent to the M-th part of the total aperture area, that is

$$\Delta A_m = \pi \left(R_m^2 - R_{m-1}^2 \right) = \frac{\pi R_{ap}^2}{M}. \quad (6)$$

The design parameter V controls the number and positions of the spiral arms created by altering the angular distance between two successive elements. With the parameter $V = 5$, this angular distance corresponds to the Golden Angle, which in conjunction with the constant ring area ΔA_m, results in an approximately uniform spatial element density, a main characteristic of the classic sunflower array [25]. Therefore, the sunflower geometry depends only on two parameters, i.e. the total number of elements M and the aperture diameter D_{ap}.

In the following, the resulting one-way PSFs for different aperture diameters and three typical fixed total numbers of elements are used to investigate the corresponding MSLLs and the MLW at $-6\,dB$ (MLW$_6$), both being widely used metrics for contrast and angular resolution (Fig. 1). The MLWs monotonously decrease with increasing aperture diameter, whereas being independent of the observed number of elements. In contrast, the MSLLs transition from a lower to a higher plateau, where there is no further significant increase. The level of the plateaus as well as the diameter at which the plateau transition occurs are both dependent on the number of elements. Therefore, if a low MSLL is desired, there is an optimal aperture diameter for each M, where the MLW is narrowest, which is just before the transition to the higher plateau.

In order to clarify the plateau-like increase in MSLL, we examine the PSF of a 64-element array for two different aperture diameters (Fig. 2). The typical one-way PSF of the classic sunflower array can be categorized into three basic zones, i.e.

1) the main lobe zone (MLZ),
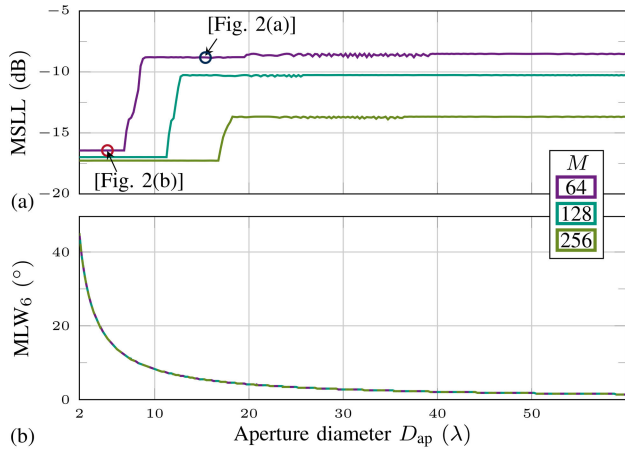2) the side lobe zone (SLZ), where low secondary lobes are formed,

FIGURE 1. MSLL (a) and MLW$_6$ (b) extracted from the normalized PSFs of classic sunflower arrays for various aperture diameters D_{ap} and three fixed numbers of elements M. While the MLW$_6$ steadily narrows with increasing aperture diameter independent of the number of elements, the MSLL features a plateau-like increase, where the transition from a low to a high plateau depends on both, the aperture diameter and the number of elements.

FIGURE 2. Two examples of 64-element classic sunflower arrays with a large ($D_{ap} = 15\,\lambda$) (a1) and a small aperture diameter ($D_{ap} = 5\,\lambda$) (b1) and their corresponding normalized PSFs (a2, b2) showing their different PSF zones. The radial view (c) shows the respective highest side lobe levels for each concentric ring with radius $R_{uv} = \sqrt{u^2 + v^2}$ centered around the PSF origin. With a sufficiently high element density, e.g. as in (b), a GLZ is not formed.

3) and the grating lobe zone (GLZ), where the side lobe level rises significantly.

The three zones are clearly evident in the radial view [Fig. 2(c)], showing the respective maximum side lobe level for each concentric ring of radius $R_{uv} = \sqrt{u^2 + v^2}$ centered on the PSF origin $(u, v) = (0, 0)$. We define the transition radius from MLZ to SLZ (R_{MLZ}) at the first minimum of the main lobe. The transition radius from SLZ to GLZ (R_{GLZ}) is specified at the side lobe level that exceeds the first, and typically highest, secondary lobe in the SLZ. We found that the MLZ transition R_{MLZ} is mainly dependent on the aperture diameter, whereas the GLZ transition (R_{GLZ}) depends on the inter-element spacings. Therefore, enlarging or reducing the aperture diameter with a fixed number of elements will narrow or widen the PSF zones, respectively. By maintaining a sufficiently small aperture, the GLZ can be forced out of the PSF, so that the MSLL decreases significantly [Fig. 2(b)]. This way, the lower MSLL plateau in Fig. 1 is reached, although with the drawback of main lobe widening.

The estimation of the positions of the three zones is of major interest for the array design. We found that for the classic sunflower array, the transition from MLZ to SLZ R_{MLZ} can be estimated with the well-known first-minimum-approximation for circular apertures [62], that is

$$R_{MLZ} \approx 1.22\lambda/D_{ap}. \tag{7}$$

The estimation of the SLZ to GLZ transition (R_{GLZ}) requires analyzing the inter-element spacings. Since most of the inter-element spacings of the classic sunflower array are different to each other, we use Delaunay triangulation [63], [64] to obtain the specific inter-element spacing between each neighboring element [Fig. 3(a)]. In [56], the authors use the
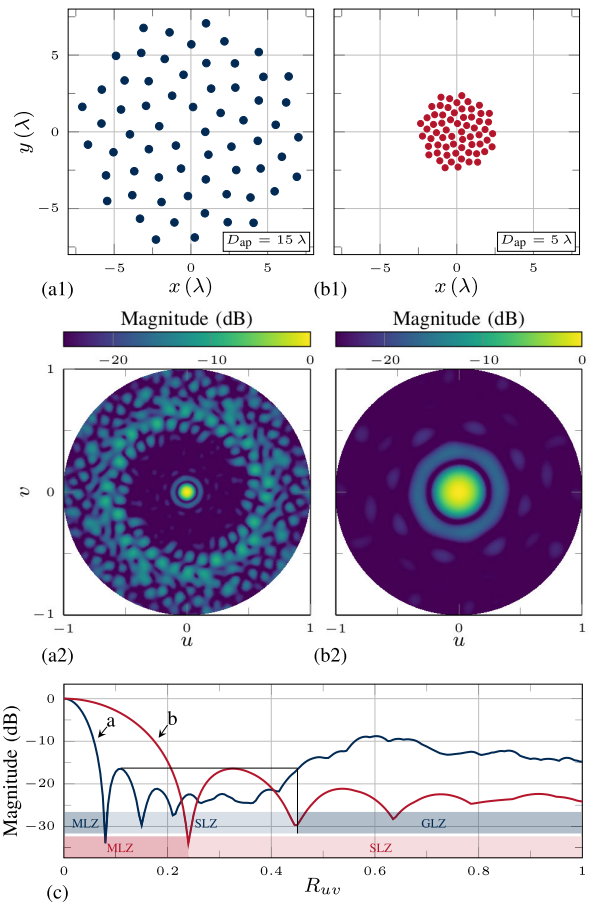
most prominent inter-element spacing $\hat{d}$ in the corresponding histogram [Fig. 3(b)], i.e. with the highest number of occurences, to estimate the position of the radius, where the highest grating lobes are located. However, we are interested in the SLZ to GLZ transition and observed that the mean inter-element spacing $\bar{d}$ gives a good estimate, that is

$$R_{GLZ} \approx \lambda/\bar{d}. \tag{8}$$

Based on this relation, we found that the classic sunflower array geometry allows to directly estimate R_{GLZ} with the basic design parameters (D_{ap}, M) as follows. We analyze the area associated to each element $A_{cell,m}$ using Voronoi tessellation and found that it is in good agreement with the M-th part of the total area just as with the circular ring area ΔA_m between two successive elements in (6). The Voronoi cell area of each element can be approximated by a circular disk with a diameter corresponding to the mean inter-element
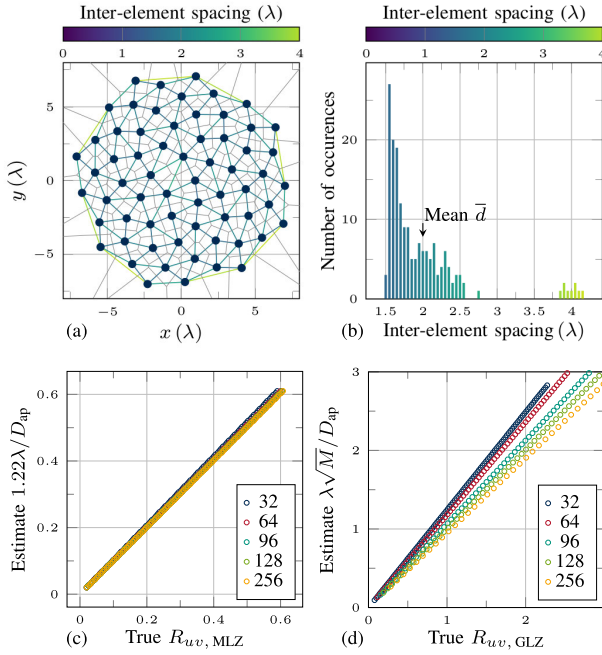
FIGURE 3. Voronoi tesselation and Delaunay triangulation applied to a 64-element classic sunflower array to find the various element cells and inter-element spacing (a) and the corresponding histogram of inter-element spacing values (b). The transition from MLZ to SLZ $R_{uv,\text{MLZ}}$ is effectively estimated with the overall aperture diameter D_{ap} (c), approximately independent of the number element. The estimation of the transition radius from SLZ to GLZ $R_{uv,\text{GLZ}}$ requires minor corrections dependent on the number of elements.

spacing, resulting in the relation

$$A_{\text{cell},m} \approx \pi \left(\frac{\overline{d}}{2} \right)^2 \approx \frac{\pi R_{\text{ap}}^2}{M} = \Delta A_m. \qquad (9)$$

Therefore, the SLZ to GLZ transition R_{GLZ} can be estimated by combining (8) and (9), that is

$$R_{\text{GLZ}} \approx \lambda \frac{\sqrt{M}}{D_{\text{ap}}}. \qquad (10)$$

We validate the approximations by determining the true respective transition radii of the classic sunflower arrays for different aperture diameters and number of elements [Fig. 3(c),(d)]. While the R_{MLZ} estimate is in good agreement with the true radii, minor correction factors h_M are required for a more precise estimation of $R_{\text{GLZ}} \approx h_M \lambda \frac{\sqrt{M}}{D_{\text{ap}}}$ depending on the number of array elements, i.e. $(h_{32}, h_{64}, h_{96}, h_{128}, h_{256}) = (0.8, 0.85, 0.94, 0.99, 1.05)$.

In order to prevent the formation of the GLZ in the PSF, as well as in beam patterns, where a source can be located off-center in a specific field-of-view within $R_{\text{fov}} = \sqrt{u^2 + v^2}$, the transition to the GLZ must be chosen to be $R_{\text{GLZ}} \geq 1 + R_{\text{fov}}$. For example, if a source can be located in a field-of-view spanning the full hemisphere

($\pm 90°$), i.e. $R_{\text{fov}} = 1$, the GLZ transition must be at least $R_{\text{GLZ}} \geq 2$ for GLZ prevention. Therefore, the aperture diameter is required to be $D_{\text{ap}} \leq 0.5\sqrt{M}\lambda$, so that the mean inter-element spacing is $\overline{d} \leq 0.5\ \lambda$, just as for the half-wavelength criterion of periodic dense arrays.

In summary, we have analyzed the MLW and the plateau-like MSLL behavior of the classic sunflower array resulting from its three PSF zones, whose locations can be estimated prior to field simulation with the aperture diameter and number of elements.

C. TWO-SCALE SPIRAL ARRAY DESIGN

The key idea leading to the proposed two-scale array design is to exploit the specific PSF zone structure of the classic sunflower array by combining two sub-arrays featuring two different spatial element densities and aperture sizes, resulting in different PSF zone locations (Fig. 4). The combination of PSF zones enables to improve and flexibly balance the MLW and MSLL, similar to density tapering, without being constrained by almost-discrete MSLL plateaus. Since we focus on the one-way beam patterns, both combined sub-arrays are used only for transmitting or only for receiving, depending on the use case. Therefore, a combination of PSF zones corresponds to a complex addition, instead of a multiplication as in the two-way case. Although, two dedicated classic sunflower arrays can be used to combine their specific far-field PSFs, nesting an inner and outer sub-array allows for a more compact design. Assigning the sub-arrays into an inner area and outer ring ensures that their element densities can be separately defined for one-way beamforming, which is more complicated for two nested sub-arrays, that both start from the center and cover a shared area, since the respective element distances are influenced by each other. Therefore, the two-scale spiral array is fully defined with four design parameters, that is

$$R_m = \begin{cases} R_{\text{in}}\sqrt{\dfrac{m}{M_{\text{in}}}}, \\ \qquad \text{for } 1 \leq m \leq M_{\text{in}}, \\ \sqrt{\dfrac{\left(R_{\text{ap}}^2 - R_{\text{in}}^2 \right)(m - M_{\text{in}})}{M - M_{\text{in}}} + R_{\text{in}}^2} \\ \qquad \text{for } M_{\text{in}} + 1 \leq m \leq M, \end{cases} \qquad (11)$$

where $R_{\text{in}} = D_{\text{in}}/2$ and $R_{\text{ap}} = D_{\text{ap}}/2$ are the inner and total aperture radius, M_{in} and M are the inner and total number of elements. The corresponding element position angles ϕ_m and the transformation into Cartesian coordinates are equivalent to (4) and (5).

In order to estimate R_{MLZ} and R_{GLZ} for both sub-arrays of the two-scale geometry, we analyze their corresponding design models. First, the radii of the inner sub-array are consistent with the classic sunflower design as in (4) using the respective inner aperture diameter D_{in} and inner number of elements M_{in}. Second, the model for the outer sub-array radii is based on the similar design rule as in (6) of the classic

sunflower geometry, i.e. the area of the ring spanned by two successive radii $\Delta A_{m,\text{out}} = \pi \left(R_m^2 - R_{m-1}^2 \right)$ is constant and equivalent to the area of the outer sub-array divided by the number of outer elements. Therefore, the inner and outer ring areas are given by

$$\Delta A_{m,\text{in}} = \frac{\pi R_{\text{in}}^2}{M_{\text{in}}}, \tag{12}$$

$$\Delta A_{m,\text{out}} = \frac{\pi (R_{\text{ap}}^2 - R_{\text{in}}^2)}{M - M_{\text{in}}}. \tag{13}$$

As a result, we obtain a composite array with only two different element densities, which are constant within each sub-array. Therefore, the two-scale array design allows to estimate the transition from SLZ to GLZ for the inner $R_{\text{GLZ, in}}$ and outer sub-array $R_{\text{GLZ, out}}$ in the same way as shown in Section II-B, that is

$$R_{\text{GLZ, in}} \approx \lambda \frac{\sqrt{M_{\text{in}}}}{D_{\text{in}}} \quad \text{and} \quad R_{\text{GLZ, out}} \approx \lambda \sqrt{\frac{M - M_{\text{in}}}{D_{\text{ap}}^2 - D_{\text{in}}^2}}. \tag{14}$$

The estimation of $R_{\text{MLZ, in}}$ and $R_{\text{MLZ, out}}$ of both sub-arrays is equivalent to (7) with the respective inner and total aperture diameters.

In summary, the ability to estimate the PSF zone locations using the basic design parameters is a major advantage of the two-scale design, since a desired PSF zone combination can be specified prior to field simulation.

D. CHARACTERISTICS OF THE TWO-SCALE SPIRAL ARRAY

Next, we examine a 64-element two-scale array to demonstrate the MLW and MSLL balancing and improvement. We focus on a geometry that exploits a specific PSF zone combination, although other advantageous combinations are possible, as shown in Section III. In particular, a GLZ-free inner sub-array with a wide MLZ is positioned within an outer sparser sub-array (Fig. 4), such that

  a) the high GLZ of the outer sparse sub-array is combined with the low SLZ of the inner sub-array, and

  b) the low SLZ of the outer sparse sub-array is paired with the MLZ and first secondary lobe of the inner sub-array,

resulting in two effects. First, the main lobes of both sub-arrays accumulate to an overall higher level and form a combined main lobe with a narrow peak and broad base. Second, the overall side lobe level is more balanced, such that there are no pronounced differences between the SLZ and GLZ, which otherwise typically consist of relatively low and high side lobe levels. Both characteristics lead to an effective reduction of the MSLL, whereas a narrow peak of the combined MLW is preserved. As a result, a higher imaging resolution with reduced artifact formation compared to the classic sunflower array is expected. Nevertheless, there is another characteristic to consider, namely the main lobe base level (approx. -11 dB in the example), where the narrow peak transitions into the broad base, whose effects are pointed out next.
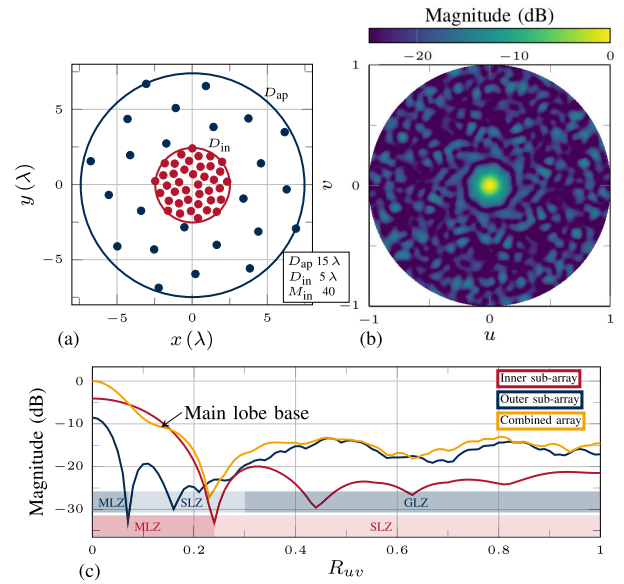

FIGURE 4. Example two-scale 64-element array nesting a denser inner sub-array with a sparser outer sub-array (a) , resulting in an advantageous PSF zone combination demonstrated in the corresponding normalized PSF (b) and its radial view (c). The combined main lobe consists of a narrow peak and broad base, whereas the overall side lobe level is more balanced without distinct transitions from SLZ to GLZ.

In order to emphasize the advantages and drawbacks of this particular two-scale spiral array, we examine the resulting beam patterns of two adjacent horizontally positioned point-sources at varying angular spacings. The beam patterns of the two-scale array and classic sunflower array are then compared, whereas both geometries are selected to have an equal -6 dB MLW (MLW_6) in their respective PSFs (Fig. 5). The angular spacing θ_s between the two adjacent positioned equal-strength point-sources is gradually increased from $0°$ to $20°$ in steps of $0.5°$. For each spacing θ_s, we generate the resulting beam patterns of the two-scale and classic sunflower array using the multi-source model in (1) with $L = 2$, where the corresponding source locations are $u_0 = +\arcsin(\theta_s/2)$ and $u_1 = -\arcsin(\theta_s/2)$. Based on these beam patterns, we evaluate the angular resolution and the minimum level between the two sources. If the minimum inter-source-level [Fig. 5(c)] drops below 0 dB, two distinct maxima are formed, such that both sources are separable in the beam pattern and the corresponding spacing defines the angular resolution.

Although both MLW_6 are equal, the two-scale array can separate the two sources at a smaller angular spacing ($6°$) compared to the classic sunflower array ($8.5°$), thus providing a higher effective angular resolution. In addition, the MSLL of the two-scale array is significantly lower (-9.86 dB vs. -4.12 dB), since the high GLZs of both sources accumulate for the classic sunflower array, increasing the risk of artifact formations. In contrast, the side lobes in the beam patterns of
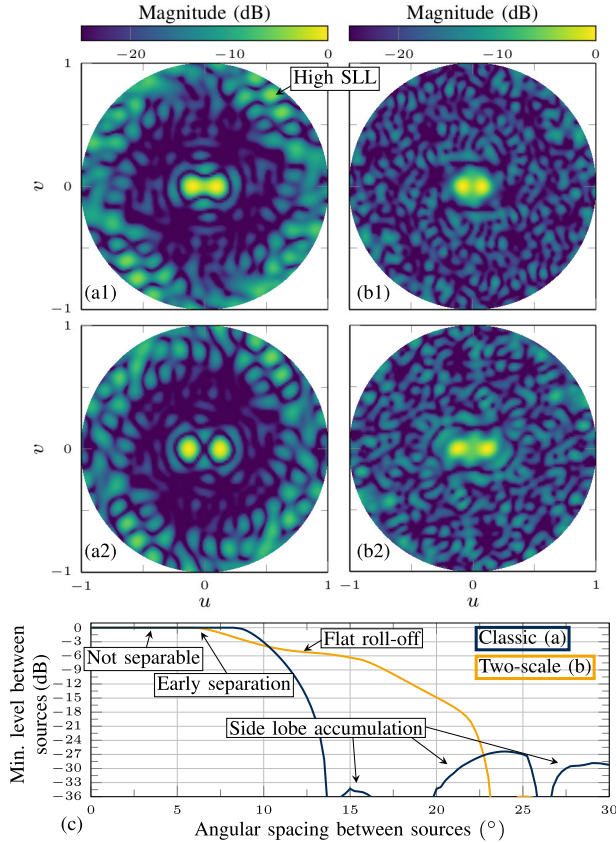
FIGURE 5. Comparison of the normalized one-way beam patterns of the classic sunflower (a) and two-scale array (b), both featuring the same $MLW_6 = 9°$, for two adjacent point sources with varying angular spacings, i.e. $10°$ (row 1) and $14°$ (row 2). Due to the accumulation of the GLZs of both sources, the resulting MSLL of (a) is significantly higher compared to (b), increasing the risk of artifact formation. The minimum side lobe level between the two sources for various spacings (c) shows that the two-scale array can separate closer-spaced sources, but requires larger spacings for a higher separation contrast due to the broad main lobe base.

the two-scale approach are more evenly distributed as in its PSF, without particularly high or low levels, so that the MSLL is kept low. However, the higher resolution and lower MSLL of the two-scale array come at a cost. Due to the wide main lobe base of the two-scale array, the minimum inter-source-level has a flatter, plateau-like roll-off with increasing source spacing compared to the classic sunflower array. Consequently, although even closely spaced sources are separable, a high separation contrast requires a larger source spacing compared to the classic sunflower array. The roll-off of the minimum inter-source level is mainly determined by the main lobe base level of the corresponding two-scale array PSF. Therefore, the main lobe base level must be considered in the two-scale array design. The re-increase of the minimum inter-source level for the classic sunflower array at $15°$ and above $20°$ angular spacing arises due to the accumulation of side lobes, which is expected behavior.

In summary, compared to the classic sunflower array with the same MLW_6, the two-scale array provides a higher angular resolution and a more effective artifact suppression due to the lower MSLL at the expense of reduced contrast between closely spaced but separable sources.

III. BENCHMARKING, RESULTS AND DISCUSSION

In this section, we benchmark the two-scale array geometries with the classic sunflower arrays and with density tapering approaches for modifying the sunflower spiral geometry. We implement two methods of density tapering for reference. One is based on a fixed window function introduced in [25] and [48], where the element positions are determined iteratively. Here, we consider a Blackman window [Fig. 6(a2)], which has been utilized in multiple previous works, e.g. [58], [59], and [58]. The other method is described by Sarradj in [61] and relies on a configurable single-parameter (H) window, based on the modified zero-th order Bessel function, where the radii of the elements are obtained by solving a non-linear least squares problem [Fig. 6(b)]. Depending on the chosen H-parameter, the Sarradj method (SAR) enables to taper the element density to the center ($H > 0$) [Fig. 6(b2)] or to the periphery of the aperture ($H < 0$) [Fig. 6(b3)]. The main difference of the density tapering methods to the two-scale array approach [Fig. 6(a3)] is that the latter does not rely on window functions, originating from amplitude apodization, but rather aims for an advantageous PSF zone combination.

In order to highlight the similarities and differences of the design methods, we compare their density window functions with respect to the non-tapered classic sunflower case. Therefore, we derive the equivalent density window function for the two-scale array, enabling to recreate the geometry introduced in this article using the density tapering method described in [25] and [48], based on the following considerations. The tapering method defines the radii R_m such that the ring area spanned by two successive radii weighted by the density window function $f(R)$ is constant (K) [25], [48], that is

$$2\pi \int_{R_{m-1}}^{R_m} f(R) R \, dR = K, \qquad (15)$$

where K is defined as the M-th part of the effective total aperture area $K = 2\pi/M \int_0^{R_{ap}} f(R) R \, dR$. For example, the equivalent density window function of the classic sunflower array is $f(R) = 1$, since the ring areas ΔA_m are already defined to be constant (6), such that

$$2\pi f(R) \int_{R_{m-1}}^{R_m} R \, dR = \pi \left(R_m^2 - R_{m-1}^2 \right) = \frac{\pi R_{ap}^2}{M}, \qquad (16)$$

where $\pi R_{ap}^2 / M = \Delta A_m = K$. Since the ring areas of the two-scale geometry ($\Delta A_{m,\text{in}}$, $\Delta A_{m,\text{out}}$) are constant within each sub-array as shown in (12) and (13), its equivalent density window function relative to the non-tapered classic

sunflower case with equal aperture diameter is given by

$$f(R) = \begin{cases} \dfrac{\Delta A_m}{\Delta A_{m,\text{in}}} = \dfrac{R_{\text{ap}}^2 M_{\text{in}}}{R_{\text{in}}^2 M}, & \text{for } 0 \leq R \leq R_{\text{in}}, \\[2ex] \dfrac{\Delta A_m}{\Delta A_{m,\text{out}}} = \dfrac{R_{\text{ap}}^2 (M - M_{\text{in}})}{(R_{\text{ap}}^2 - R_{\text{in}}^2)M}, & \text{for } R_{\text{in}} < R \leq R_{\text{ap}}. \end{cases}$$

$$(17)$$

Therefore, the equivalent density window function of the two-scale array consists of two discrete density levels in contrast to the Blackman and SAR tapering methods, which feature a smooth characteristic [Fig. 6(c)]. Besides that, the similarities of the Blackman and SAR tapering methods become evident in the comparison. The SAR window functions with $H = 1$ and $H = 4$ lead to a respectively weaker and stronger inner tapering compared to the Blackman window, which is approximately identical to SAR $H = 2.5$. In fact, many spiral array geometries are contained in the set of solutions created by the SAR method for varying H parameters, including the classic sunflower array, which results for $H = 0$.

A. DESIGN METHODS BENCHMARKING

For benchmarking, we generate different array geometries with a fixed number of elements ($M = 64$ and $M = 256$) based on the four design methods presented, each with varying design parameters. The aperture diameter, which is the only variable parameter for the classic sunflower and the Blackman density tapered array, is varied in the interval $D_{\text{ap}} \in \{2, 3, \ldots, 60\}\lambda$. For each aperture diameter, the H-parameter of the SAR arrays are additionally varied within $H \in \{-5, -4.8, \ldots, 5\}$. The two-scale array geometries are created using any combination of D_{ap} with the remaining two variable parameters, i.e. inner diameter D_{in} and inner number of elements M_{in}, in the intervals $M_{\text{in}} \in \{1, 2, \ldots, M-1\}$ and $D_{\text{in}} \in \{[1, 2, \ldots, 59]\lambda \mid D_{\text{in}} < D_{\text{ap}}\}$. The interval boundaries for the parameter sweep are chosen to be comparable to existing literature, e.g. as in [61].

Subsequently, the corresponding PSF for each array geometry is formed from which the performance metrics, i.e. MLW_6 and MSLL, are automatically extracted. We use the MSLL as it reflects the worst-case metric in the formation of side lobe artifacts. In order to consider the side lobes that are created by an off-center point-source located within the full-hemisphere field-of-view as well, we evaluate the PSF within $R_{\text{uv}} = \sqrt{u^2 + v^2} \leq 2$ instead of ≤ 1. For clear comparison, we select and show only the optimum arrays with the lowest MSLL per MLW_6 of each approach. Here, we do not consider two-scale arrays with an main lobe base level above $-9\,\text{dB}$. Otherwise, the comparison would be clearly in favor of two-scale arrays with a narrow MLW_6 but poor separation contrast for closely spaced sources (Section II-D). The MLW_6 and MSLL of the selected arrays of all approaches are then compared (Fig. 7). First, we conside the array geometries using 64 elements.
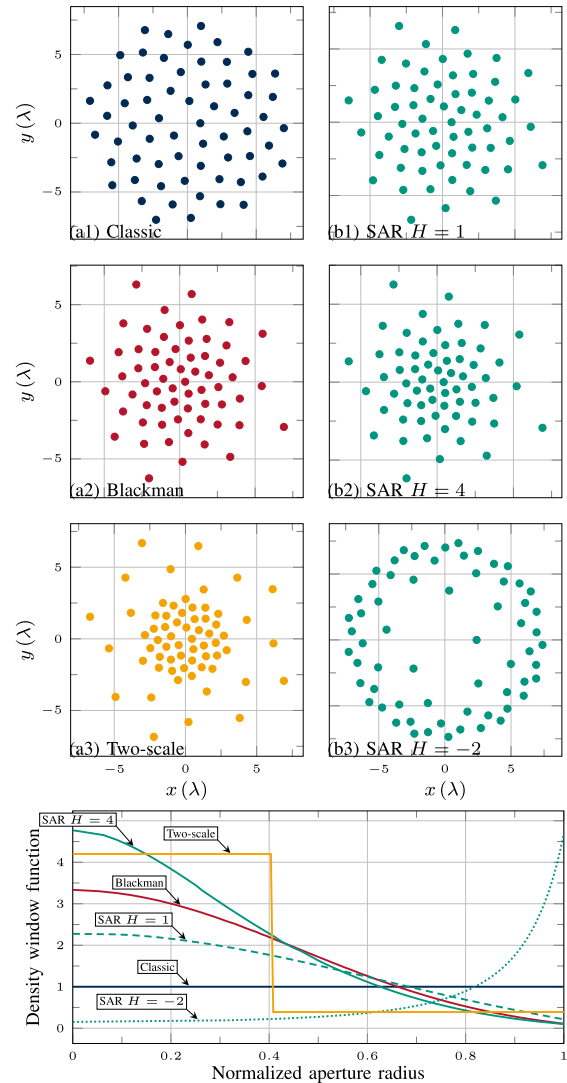

FIGURE 6. Comparison of example geometries of the design methods used for the benchmark, i.e. the classic sunflower array (a1), different spatial density tapering modifications based on a fixed Blackman window (a2) [25], [48] and the approach of Sarradj [61] using a parametric (H) density window function (b) , as well as the two-scale method proposed in this article (a3). The SAR method allows a flexible modification by varying the H parameter, e.g. for peripheral tapering (b3). The density window functions (c) show the density taper relative to the non-tapered classic sunflower case and emphasize the differences and similarities of the methods.

The classic sunflower arrays provide the reference baseline for the comparison. Their characteristic MSLL plateaus at approximately $-8.8\,\text{dB}$ and $-16.5\,\text{dB}$ including their steep transition are clearly noticeable, similar as in (Fig. 1).

The Blackman window density tapering approach has, to some extent, a lower MSLL for the same MLW_6, particularly between $14°$ and $21°$, where a MSLL improvement from $-8.8\,\text{dB}$ down to $-11.5\,\text{dB}$ is observed. In addition, the MSLL can be further reduced below the lower plateau of the classic sunflower approach for MLWs wider than $32°$.
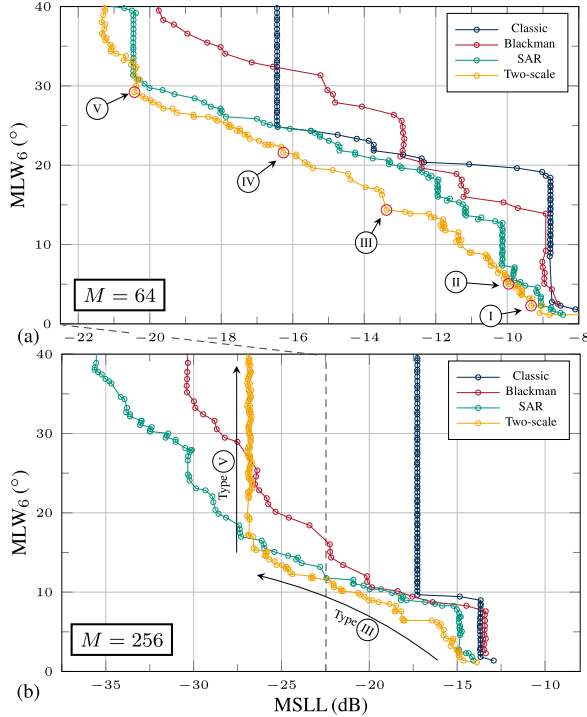
FIGURE 7. Benchmark of the four design methods showing the resulting one-way PSF quality metrics of the optimum arrays of each approach with a fixed number of elements (64 (a) and 256 (b)) and varying design parameters. Sources located off-center in the entire hemisphere (field-of-view of ±90°) are considered for MSLL evaluation. The optimum 64-element arrays of the two-scale method include five different types of PSF zone combinations (I to V), all of which feature improved or similar MLW and MSLL compared to the other approaches. Similar results are obtained for 256-element arrays, although the two-scale approach provides no further MSLL improvement for main lobe widths wider than 15°.

The SAR arrays generally outperform the classic sunflower and Blackman window method as expected, since they are a subset of the SAR geometries. The variation of the H parameter enables a more flexible balancing between MLW and MSLL, e.g. with peripheral density tapering. This way, the performance gaps of the Blackman approach are overcome.

Finally, the two-scale array design provides the lowest MSLLs for most MLWs compared to the previous approaches, although the MSLLs for rather narrow or wide MLWs (e.g. $< 7°$ and $> 31°$) are similar to the SAR density tapering method. In general, similar results are obtained for the 256-element array geometries, where the classic sunflower method shows two distinct MSLL plateaus, the SAR technique outperforms the Blackman approach, and the two-scale geometries provide lower or similar MSLL per MLW compared to the SAR method. However, for wide MLWs above 15°, the two-scale approach reaches a plateau and stops to improve the MSLL at approximately -27 dB, whereas it can be further lowered by the Blackman and SAR technique.

Clearly, there are specific PSF zone combinations that lead to particularly effective improvements, while others perform only similarly or worse compared to previous density tapering approaches. For example, one of the greatest improvements for the 64-element geometries occurs for an MLW of 14°, where the MSLL of the two-scale approach (-13.4 dB) is significantly lower than for the classic sunflower (-8.8 dB) or SAR (-11.1 dB) method. In fact, this particular two-scale array utilizes the PSF zone combination (Type III) analyzed in Section II-D. Overall, five different types (I to V) of advantageous PSF zone combinations are observed in the set of optimum 64-element two-scale arrays, which are examined next.

B. OPTIMUM TWO-SCALE ARRAY COMBINATION TYPES

The first type [Fig. 8(I)], consists of a large-aperture outer sub-array which includes most of the available elements, and, therefore, predominantly determines the PSF. In contrast, the contribution of the inner sparser sub-array is only supportive by adding to the relative main lobe level and by positioning its first secondary lobe (SL) minimum close to the first high side lobe of the outer sub-array.

Type two [Fig. 8(II)], features a more balanced distribution of the inner and outer number of elements, although the latter is still dominant. Most importantly, the inner and outer aperture diameters D_{in} and D_{ap} differ only slightly. This way, a denser outer ring sub-array is formed filled by a sparser inner sub-array. As a result, both MLWs are similar to each other and accumulate without significant widening. The low SLZ of the sparse inner sub-array is positioned near the highest side lobes of the outer array, equalizing the overall side lobe level. In general, this type is similar to the peripheral density tapering of the SAR approach, e.g. for $H = -2$ [Fig. 6(b3)].

The third type [Fig. 8(III)] is the basis of the original idea for the two-scale array design, outlined in the previous sections. Here, the distribution of the number of elements is balanced as well, with the inner sub-array being denser and more populated. Basically, the densities of the inner and outer sub-arrays are inverted compared to type II, resulting in a different PSF zone combination, as depicted in Section II-D. The MSLL is significantly reduced compared to the other approaches given the same MLW_6. Still, there is the drawback of reduced contrast between closely spaced sources. The optimum 256-element two-scale array geometries, which provide improved results compared to the previous approaches, consist exclusively of this type III.

In type four [Fig. 8(IV)], the PSF is primarily determined by the inner denser sub-array, while few outer sparse elements contribute only as support for balancing out the side lobe level, forming the counterpart to type I.

Finally, in type five [Fig. 8(V)], the sub-arrays differ only slightly in spatial density and therefore resemble the classic sunflower array more closely compared to the previous types. Nevertheless, even the small differences cause the side lobe minima and maxima to balance each other out, resulting in a
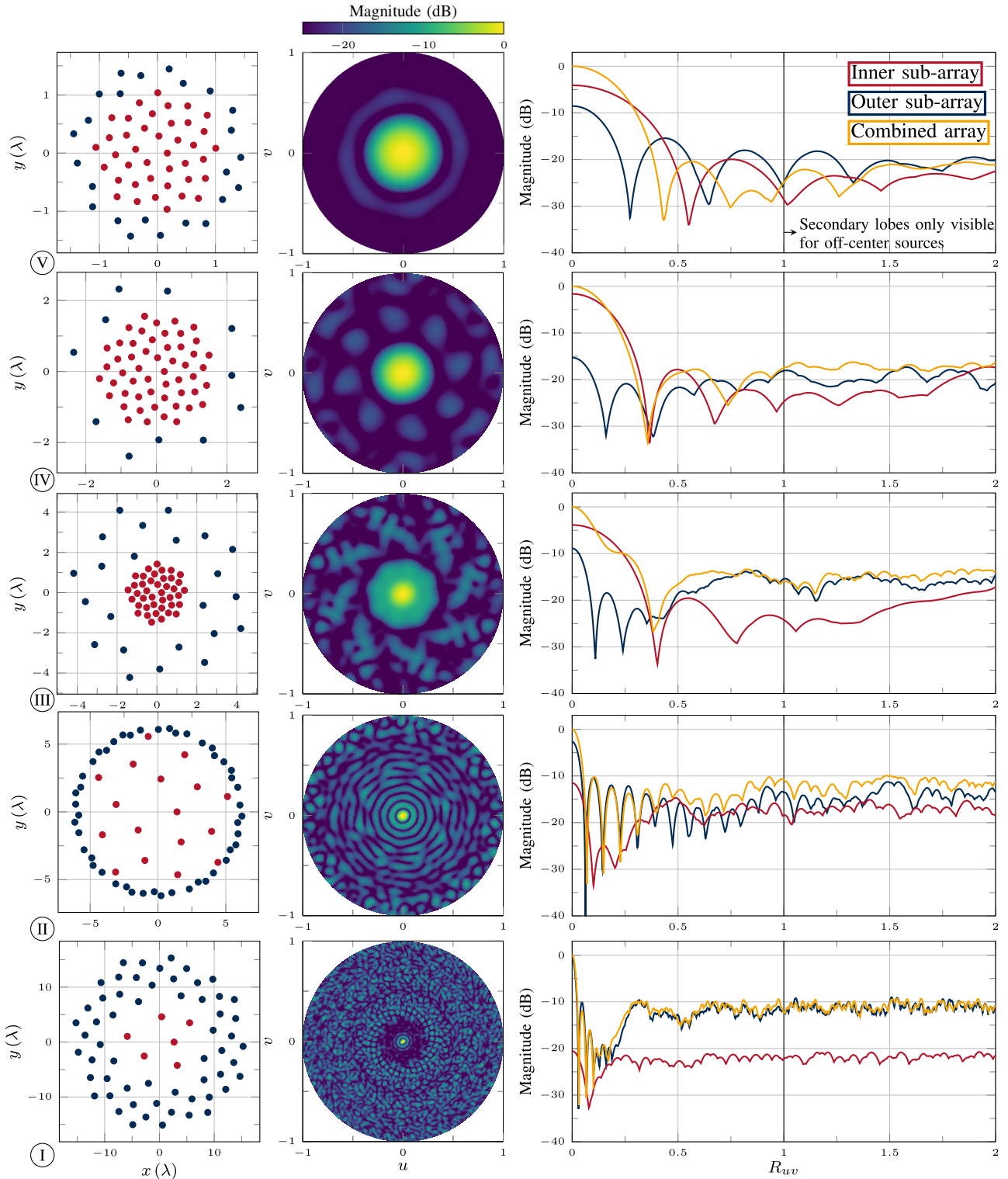
FIGURE 8. Five different types of advantageous sub-array combinations observed in the set of optimum two-scale arrays (Fig. 7). Type I and IV feature either a dominant outer or inner sub-array, whereas the opposite sub-array is only supportive. In II and III, the ratio between inner and outer elements is more balanced and the sub-arrays are of different spatial densities for exploiting the PSF zone combinations. In particular, type III shows significant improvements compared to other design methods as examined in the previous sections. The sub-arrays of type V have only minor differences in spatial densities, which nevertheless result in an effective positioning of the side lobe minima and maxima for a more balanced overall side lobe level.

significantly lower MSLL compared to the classic sunflower approach. However, compared to the previous density tapering approaches, type V provides only similar or worse results, particularly for the 256-element arrays.

In summary, considering the progression from wide to narrow MLWs, the optimum two-scale arrays feature an increasing overall aperture, as well as a shift from type I to V ($M = 64$) or type III to V ($M = 256$), respectively. For all optimum combinations, the corresponding sub-array main lobes accumulate to a higher level, whereas the overall side lobe level becomes more balanced compared to the classic sunflower approach. The most effective improvements over the existing density tapering approaches are achieved, where a dense inner sub-array is combined with a sparse outer sub-array, with a balanced number of inner and outer elements, as in type III. In contrast, for rather small apertures, where both sub-arrays are dense and grating lobe zones do not form (type V), the two-scale PSF zone combination is less effective. In this case, although significant improvements over the classic sunflower array are achieved, the two-scale results can be similar or even inferior compared to the Blackman and SAR method.

C. BENCHMARK WITH EXTENDED ELEMENT APERTURES

In the preceding analysis, unidirectional point elements with infinitely small aperture sizes are assumed to provide a generic technology-independent comparison. In order to highlight the impact of extended element apertures, in this section, we compare the array design methods, assuming circular elements with a diameter of $D_{ap,el} = \lambda/2$, as an example. Here, we consider two resulting effects. First, the minimum IES is limited to $d = D_{ap,el}$, such that non-realizable array geometries featuring overlapping elements are discarded. Second, the element directivity itself leads to a degradation of the MSLL, when spatial filtering for peripheral directions. Regarding the latter, we consider spatial filtering and source positioning in the entire hemisphere, i.e. within a field of view of ±90°, as in the preceding comparison (Fig. 7). The element directivity is modeled as described in section II-A. The design parameter space investigated is identical as described in section III-A and two different numbers of elements are observed, i.e. $M = 64$ and $M = 256$.

As expected, the resulting MLWs show an upper limit because the array apertures can not become arbitrarily small due to the extended elements (Fig. 9). The worst-case MSLLs of the optimum array geometries are approximately 3 dB higher compared to the analysis based on point elements due to MSLL degradation resulting from the element directivity and the considered field-of-view. Furthermore, an increase in MLW partly leads to a degradation of the MSLL, which is shown as an example for the classic spiral and Blackman geometries. The reason is that for these non-optimum array geometries, the highest side lobes are located near the center, as the main lobe is steered to the periphery and, thus,
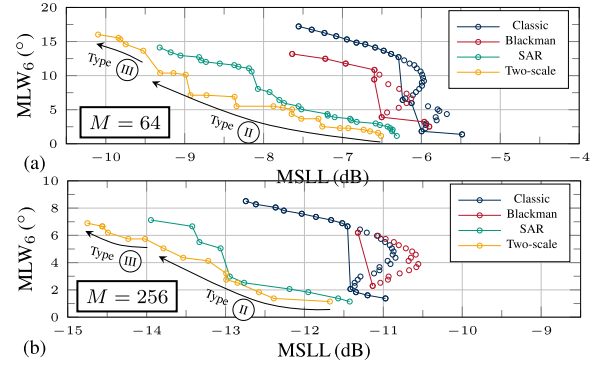

FIGURE 9. Benchmark of the four design methods for extended circular element apertures with a diameter of 0.5 λ. The comparison considers spatial filtering and source positioning in the entire hemisphere (field-of-view of ±90°). As the minimum realizable array aperture is constrained by the element sizes, the MLWs show an upper limit. Due to the element directivities, there are non-optimum array geometries, where the MSLL worsens with increasing MLW, which are included as an example for the classic and Blackman method.

attenuated by the element directivity. All in all, the comparison highlights that the SAR and two-scale geometries perform comparably well when assuming extended element apertures, whereas the latter design method provides the lowest MSLL per MLW, as in the comparison assuming point elements (Fig. 7). The optimum two-scale array geometries observed correspond to the types II and III, but feature an overall larger total aperture compared to the example in (Fig.8), so that the IES of the outer or inner denser sub-arrays are consistently greater than 0.5 λ.

D. SCOPE AND LIMITATIONS OF THE STUDY

In this final section of the theoretical study, we highlight the scope and limitations of the analysis and results. As explained in Section II, the analysis is performed using a generic application-independent model, assuming far-field and narrow-band conditions, i.e. continuous wave or temporally long bursts, such that the comparison is based on worst-case assumptions. However, in the near-field case, the results obtained with focused beams may differ from the far-field results provided, depending on the application-specific focal distance and region of interest. Further deviations from the comparison results are likely to occur, if high-bandwidth transducer technologies and temporally short pulses are involved, that enable to exploit true-time-delay and broad-band beamforming methods for reducing side lobe levels. In addition, even larger element sizes than the example size considered can further constrain the realizable array geometries, so that the outcomes of the comparison may also vary for this reason. Consequently, the results presented are not directly valid for all applications, particularly if the base conditions in terms of element size and shape, bandwidth, focal distance and region of interest differ significantly from the model assumptions used.

Apart from the limitations due to the generic model, we emphasize that further modifications and optimization
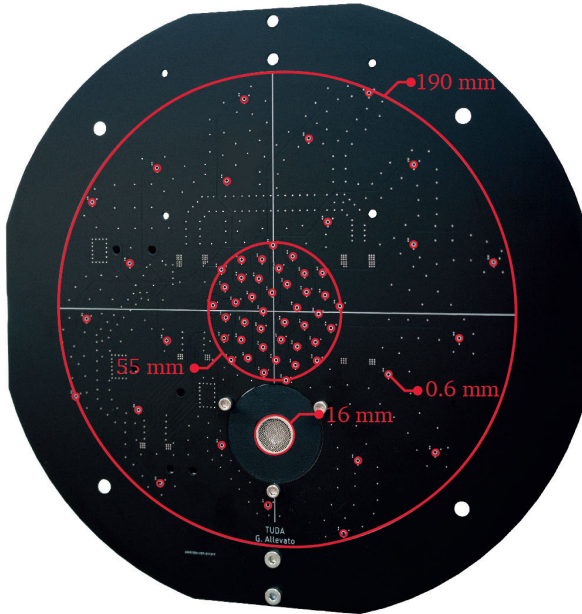
FIGURE 10. Two-scale array prototype for in-air imaging consisting of one 32.8-kHz piezoelectric ultrasonic transducer and 64 MEMS microphones, divided into a 40-element inner and 24-element outer sub-array. The microphones are approximately unidirectional and broad-band, whereas the transducer is highly narrow-band (4.3%).
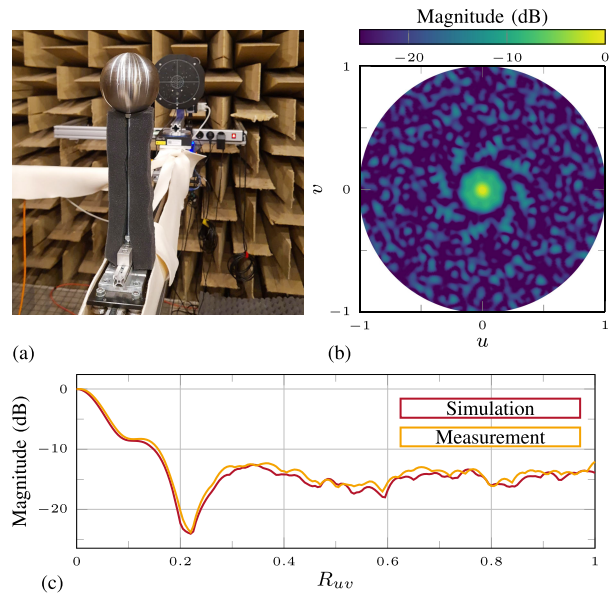

FIGURE 11. Measurement setup in the anechoic chamber (a) for investigating the PSF in the far-field (2 m). The target used is a hollow steel sphere with a diameter of 10 cm. The PSF measured (b) and its radial view (c) are in good agreement with the corresponding simulation, highlighting the narrow main lobe peak and balanced side lobe level.

procedures can certainly lead to improved solutions compared to those investigated within the parameter space of the study. For example, adding more than two sub-arrays with different element densities can potentially provide further improvements at the expense of a more complicated array design including more parameters. Moreover, the well-performing deterministic two-scale solutions identified can be used as initial seeds for further stochastic optimization methods. Nevertheless, these improvement strategies are beyond the scope of this article and are worthy ideas for future work.

IV. REAL-WORLD EXPERIMENTS

In this section, we validate the two-scale array design strategy with a real-world prototype and two experiments in order to investigate the PSF and the resulting angular resolution.

For this, we created an air-coupled two-scale array based on type III, consisting of 64 small MEMS microphones (Knowles SPH0641LU4H-1) featuring a digital interface. In addition, we utilize one piezoelectric bending-plate transducer (ProWave 328ST160) with a diameter of 16 mm and a relatively low resonance frequency of 32.8 kHz to avoid strong attenuation by the medium air (Fig. 10). The frequency response of the transducer is narrow-band (1.4 kHz, 4.3%), so that a temporally long excitation signal (40 cycles, 70 V_{pp}, bipolar square-wave) is required, which, however, enables the pulse to reach a relatively high sound pressure level of 123 dB at a distance of 30 cm. Therefore, the narrow-band assumption holds for this prototype and the experiments. The microphones are broadband (10 Hz to 80 kHz), compact

($3.5 \times 2.6 \times 1\,mm^3$) and approximately unidirectional due to the small aperture diameter of 0.325 mm (0.03 λ). The ports of the microphones are located on the bottom side and are guided through the PCB with a thickness of 1.6 mm by using vias with a diameter of 0.6 mm. The microphones each provide a 4-MHz 1-bit PDM signal, all of which are converted into 125-KHz 16-bit signals by an FPGA (Intel MAX10) using 64 sinc-3 filters. The system architecture is based on the design described in detail in our previous work [3]. The type III two-scale array geometry is composed of the inner denser sub-array with 40 elements and an aperture diameter of 55 mm, while the outer sub-array consists of 24 elements and spans a total aperture of 190 mm. The implementation of signal pre-processing, narrow-band receive beamforming and image formation is described in detail in [65].

The experiments are conducted in an anechoic chamber, where the two-scale array is positioned in front of a linear axis equipped with a movable slide. In order to measure the PSF, we use a hollow steel sphere ($\varnothing 10\,cm$) as target, which is mounted on a sound-absorbing fixture and positioned on the slide at a distance of 2 m, i.e. in the far-field, centered to the array. The pulse is transmitted to the sphere, its echo is received by all microphones and the PSF is formed at the pulse maximum within the field-of-view $R_{uv} = \sqrt{u^2 + v^2} \leq 1$ (Fig. 11). This measurement is repeated 32 times to obtain the average value and the standard deviation. The latter is consistently below 0.1 dB and is therefore excluded for clarity. Furthermore, the PSF measured is compared to the ideal simulation based on the model in (1).
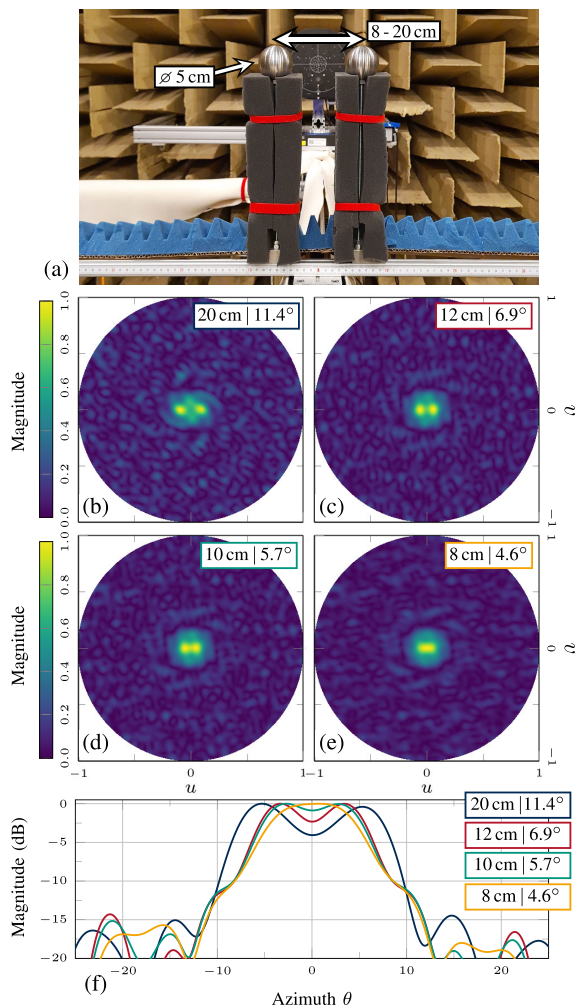
FIGURE 12. Measurement setup for investigating the angular resolution (a) using two spheres. The spacing between the spheres is gradually reduced and the separability of the two reflections is evaluated in the ultrasound images (b)-(e). In the horizontal sectional view (f), the closest separable spacing is 10 cm (5.7°), as two distinct local maxima are formed.

The measured and simulated PSFs are in excellent agreement, with the measurement featuring a slightly higher MSLL (-12.1 dB vs. -12.6 dB) and a wider MLW (8.05° vs. 7.47°) compared to the simulation. Overall, both, the balanced side lobe level, as well as the distinctive shape of the main lobe due to the combination of the two sub-arrays, are evident, as expected.

In the next experiment, the achievable angular resolution is investigated, comparable to the simulation in (Fig. 5). For this, a horizontal mounting is positioned on the slide, onto which two laterally adjacent hollow spheres ($\varnothing 5$ cm) are attached, whose spacing between each other can be variably adjusted (Fig. 12). The sphere fixtures and the horizontal mounting are covered with sound absorbers as well. The slide is positioned at a fixed distance of 1 m (far-field) and the spacing between the spheres is symmetrically reduced from 20 cm to 8 cm in steps of 2 cm. At each spacing, an image is formed to evaluate the separability of the two sphere reflections. The

separability is achieved if the two sphere reflections form two distinct local maxima in the image. As an example, four ultrasound images with different sphere spacings are provided, as well as their horizontal sectional view at $v = 0$ (Fig. 12).

As the angular spacing between the spheres decreases, the local minimum between the two reflections increases in good agreement to the simulation (Fig. 5). The MSLL is between -10 dB (at 11.4°) and -12.25 dB (at 4.6°) for all spacings considered. Due to the narrow main lobe peak, the closest separable angular distance is 5.7°, which corresponds to a spacing of 10 cm between the spheres. In total, the real-world experiments using the two-scale prototype created confirm the results of the simulation and demonstrate that the two-scale design provides a favorable trade-off between the separation of closely spaced objects and a low MSLL.

V. CONCLUSION AND OUTLOOK

The two-scale sparse spiral array is based on a deterministic and flexible 4-parameter design method for improving the one-way PSF performance in terms of MLW and MSLL compared to previous sunflower geometry modification approaches, i.e. density tapering using window function. The improvements are achieved by exploiting the sunflower-specific PSF structures of two nested sub-arrays featuring two different spatial element densities which are constant within each sub-array. This way, the PSF zone locations can be estimated prior to field simulation using the basic array design parameters, enabling to narrow the search for well-matched array configurations within pre-defined design constraints. Due to the excellent one-way PSF characteristics, the two-scale method proposed is particularly valuable for imaging applications, where high frame rates are of great importance, as well as for transmit- and receive-only applications. Future work addresses the impact of additional density tapering on the two-scale sub-arrays, potentially enabling further improvement. In addition, we evaluate whether the two-scale array achieves favorable results in the two-way beamforming mode as well, e.g. by using the inner and outer sub-arrays separately for transmitting and receiving. Moreover, we extend the prototype in terms of transducer technology and firing schemes in synergy with the two-scale design strategy to achieve further improvements for high-frame rate imaging in air and conduct additional experimental evaluations.

REFERENCES

[1] R. Kerstens, D. Laurijssen, and J. Steckel, "ERTIS: A fully embedded real time 3D imaging sonar sensor for robotic applications," in *Proc. Int. Conf. Robot. Autom. (ICRA)*, May 2019, pp. 1438–1443.

[2] J. Steckel, A. Boen, and H. Peremans, "Broadband 3-D sonar system using a sparse array for indoor navigation," *IEEE Trans. Robot.*, vol. 29, no. 1, pp. 161–171, Feb. 2013.

[3] G. Allevato, M. Rutsch, J. Hinrichs, M. Pesavento, and M. Kupnik, "Embedded air-coupled ultrasonic 3D sonar system with GPU acceleration," in *Proc. IEEE SENSORS*, Oct. 2020, pp. 1–4.

[4] C. A. Andersen, S. Holden, J. Vela, M. S. Rathleff, and M. B. Jensen, "Point-of-care ultrasound in general practice: A systematic review," *Ann. Family Med.*, vol. 17, no. 1, pp. 61–69, Jan. 2019.

[5] R. Bharath, D. S. Reddy, and P. Rajalakshmi, "A SoC-based programmable portable ultrasound scanning system for point-of-care applications and clinical research activities," *Social Netw. Comput. Sci.*, vol. 3, no. 5, p. 349, Jun. 2022.

[6] J. H. Song, J. Lee, S. Yeo, G.-D. Kim, and T.-K. Song, "An analytical approach to designing optimal sparse 1-D phased arrays for handheld ultrasound imaging," *IEEE Trans. Ultrason., Ferroelectr., Freq. Control*, vol. 67, no. 7, pp. 1354–1365, Jul. 2020.

[7] D. H. Turnbull and F. S. Foster, "Beam steering with pulsed two-dimensional transducer arrays," *IEEE Trans. Ultrason., Ferroelectr., Freq. Control*, vol. 38, no. 4, pp. 320–333, Jul. 1991.

[8] A. Ramalli, E. Boni, E. Roux, H. Liebgott, and P. Tortoli, "Design, implementation, and medical applications of 2-D ultrasound sparse arrays," *IEEE Trans. Ultrason., Ferroelectr., Freq. Control*, vol. 69, no. 10, pp. 2739–2755, Oct. 2022.

[9] J. A. Jensen et al., "Anatomic and functional imaging using row-column arrays," *IEEE Trans. Ultrason., Ferroelectr., Freq. Control*, vol. 69, no. 10, pp. 2722–2738, Oct. 2022.

[10] B. Diarra et al., "Feasibility of genetic algorithms in 2D ultrasound array optimization," in *Proc. IEEE Int. Ultrason. Symp. (IUS)*, Oct. 2018, pp. 1–9.

[11] K. Chen, X. Yun, Z. He, and C. Han, "Synthesis of sparse planar arrays using modified real genetic algorithm," *IEEE Trans. Antennas Propag.*, vol. 55, no. 4, pp. 1067–1073, Apr. 2007.

[12] A. Austeng, S. Holm, P. K. Weber, N. Aakvaag, and K. Iranpour, "1D and 2D algorithmically optimized sparse arrays," in *Proc. IEEE Ultrason. Symp.*, Oct. 1997, pp. 1683–1686.

[13] R. L. Haupt, "Thinned arrays using genetic algorithms," *IEEE Trans. Antennas Propag.*, vol. 42, no. 7, pp. 993–999, Jul. 1994.

[14] E. Roux, A. Ramalli, P. Tortoli, C. Cachard, M. C. Robini, and H. Liebgott, "2-D ultrasound sparse arrays multidepth radiation optimization using simulated annealing and spiral-array inspired energy functions," *IEEE Trans. Ultrason., Ferroelectr., Freq. Control*, vol. 63, no. 12, pp. 2138–2149, Dec. 2016.

[15] C. Sciallero and A. Trucco, "Design of a sparse planar array for optimized 3D medical ultrasound imaging," in *Proc. 23rd Eur. Signal Process. Conf. (EUSIPCO)*, Aug. 2015, pp. 1341–1345.

[16] B. Diarra, M. Robini, P. Tortoli, C. Cachard, and H. Liebgott, "Design of optimal 2-D nongrid sparse arrays for medical ultrasound," *IEEE Trans. Biomed. Eng.*, vol. 60, no. 11, pp. 3093–3102, Nov. 2013.

[17] A. Trucco, "Thinning and weighting of large planar arrays by simulated annealing," *IEEE Trans. Ultrason., Ferroelectr., Freq. Control*, vol. 46, no. 2, pp. 347–355, Mar. 1999.

[18] M. Karaman, I. O. Wygant, O. Oralkan, and B. T. Khuri-Yakub, "Minimally redundant 2-D array designs for 3-D medical ultrasound imaging," *IEEE Trans. Med. Imag.*, vol. 28, no. 7, pp. 1051–1061, Jul. 2009.

[19] A. Austeng and S. Holm, "Sparse 2-D arrays for 3-D phased array imaging-design methods," *IEEE Trans. Ultrason., Ferroelectr., Freq. Control*, vol. 49, no. 8, pp. 1073–1086, Aug. 2002.

[20] S. I. Nikolov and J. A. Jensen, "Application of different spatial sampling patterns for sparse array transducer design," *Ultrasonics*, vol. 37, no. 10, pp. 667–671, Jul. 2000.

[21] S. S. Brunke and G. R. Lockwood, "Broad-bandwidth radiation patterns of sparse two-dimensional Vernier arrays," *IEEE Trans. Ultrason., Ferroelectr., Freq. Control*, vol. 44, no. 5, pp. 1101–1109, Sep. 1997.

[22] H. Vogel, "A better way to construct the sunflower head," *Math. Biosci.*, vol. 44, nos. 3–4, pp. 179–189, Jun. 1979.

[23] D. W. Boeringer, "Phased array including a logarithmic spiral lattice of uniformly spaced radiating and receiving elements," U.S. Patent 6 433 754 B1, Aug. 13, 2002.

[24] F. Vidal, H. Legay, G. Goussetis, and A. Segneri, "A system approach to enable digital beamforming with direct radiating arrays: The joint use of precoding and sparse arrays," *Int. J. Satell. Commun. Netw.*, vol. 39, no. 6, pp. 645–660, Nov. 2021.

[25] M. C. Viganó, G. Toso, G. Caille, C. Mangenot, and I. E. Lager, "Sunflower array antenna with adjustable density taper," *Int. J. Antennas Propag.*, vol. 2009, pp. 1–10, Jan. 2009.

[26] O. Christogeorgos, H. Zhang, Q. Cheng, and Y. Hao, "Extraordinary directive emission and scanning from an array of radiation sources with hyperuniform disorder," *Phys. Rev. Appl.*, vol. 15, no. 1, Jan. 2021, Art. no. 014062.

[27] Q. Cheng, Y. Liu, H. Zhang, and Y. Hao, "A generic spiral MIMO array design method for short-range UWB imaging," *IEEE Antennas Wireless Propag. Lett.*, vol. 19, no. 5, pp. 851–855, May 2020.

[28] J. Wang, P. Aubry, and A. Yarovoy, "3-D short-range imaging with irregular MIMO arrays using NUFFT-based range migration algorithm," *IEEE Trans. Geosci. Remote Sens.*, vol. 58, no. 7, pp. 4730–4742, Jul. 2020.

[29] Y. Aslan, J. Puskely, J. H. J. Janssen, M. Geurts, A. Roederer, and A. Yarovoy, "Thermal-aware synthesis of 5G base station antenna arrays: An overview and a sparsity-based approach," *IEEE Access*, vol. 6, pp. 58868–58882, 2018.

[30] J. Liao et al., "Beam-quality improvement with a bio-inspired sunflower array for coherent beam combining," *Appl. Opt.*, vol. 60, no. 31, p. 9713, Nov. 2021.

[31] R. S. Cardoso, L. P. Oliveira, and H. E. Hernandez-Figueroa, "Assessment of Fermat's spiral arrays for photonic dielectric antennas," in *Proc. 15th Eur. Conf. Antennas Propag. (EuCAP)*, Mar. 2021, pp. 1–4.

[32] J. L. Pita, I. Aldaya, O. J. S. Santana, L. E. E. De Araujo, P. Dainese, and L. H. Gabrielli, "Side-lobe level reduction in bio-inspired optical phased-array antennas," *Opt. Exp.*, vol. 25, no. 24, p. 30105, Nov. 2017.

[33] L. H. Gabrielli and H. E. Hernandez-Figueroa, "Aperiodic antenna array for secondary lobe suppression," *IEEE Photon. Technol. Lett.*, vol. 28, no. 2, pp. 209–212, Jan. 15, 2016.

[34] S. Jekosch and E. Sarradj, "An inverse microphone array method for the estimation of a rotating source directivity," *Acoustics*, vol. 3, no. 3, pp. 462–472, Jun. 2021.

[35] C. VanDercreek, R. Merino-Martinez, M. Snellen, and D. Simons, "Comparison of cavity geometries for a microphone array in an open-jet wind-tunnel experiment," in *Proc. 8th Berlin Beamforming Conf.*, Mar. 2020, pp. 1–3.

[36] S. Luesutthiviboon, A. Malgoezar, M. Snellen, P. Sijtsma, and D. Simons, "Improving source discrimination performance by using an optimized acoustic array and adaptive high-resolution CLEAN-SC beamforming," in *Proc. 7th Berlin Beamforming Conf.*, 2018, pp. 1–27.

[37] A. Price and B. Long, "Fibonacci spiral arranged ultrasound phased array for mid-air haptics," in *Proc. IEEE Int. Ultrason. Symp. (IUS)*, Oct. 2018, pp. 1–4.

[38] B. Parr, M. Legg, S. Bradley, and F. Alam, "Occluded grape cluster detection and vine canopy visualisation using an ultrasonic phased array," *Sensors*, vol. 21, no. 6, p. 2182, Mar. 2021.

[39] M. Legg and S. Bradley, "Ultrasonic arrays for remote sensing of pasture biomass," *Remote Sens.*, vol. 12, no. 1, p. 111, Dec. 2019.

[40] G. Allevato et al., "Air-coupled ultrasonic spiral phased array for high-precision beamforming and imaging," *IEEE Open J. Ultrason., Ferroelectr., Freq. Control*, vol. 2, pp. 40–54, 2022.

[41] G. Allevato, M. Rutsch, J. Hinrichs, E. Sarradj, M. Pesavento, and M. Kupnik, "Spiral air-coupled ultrasonic phased array for high resolution 3D imaging," in *Proc. IEEE Int. Ultrason. Symp. (IUS)*, Sep. 2020, pp. 1–4.

[42] A. R. K. Towlson, A. J. Croxford, and B. W. Drinkwater, "Ultrasonic nondestructive characterization of blockages and defects in underground pipes," *IEEE Trans. Ultrason., Ferroelectr., Freq. Control*, vol. 69, no. 8, pp. 2540–2554, Aug. 2022.

[43] X. Qu et al., "Suppressing grating lobes for transcranial focused ultrasound system by frequency-modulated excitation," *IEEE Trans. Ultrason., Ferroelectr., Freq. Control*, vol. 68, no. 2, pp. 341–351, Feb. 2021.

[44] C. R. Bawiec et al., "A prototype therapy system for boiling histotripsy in abdominal targets based on a 256-element spiral array," *IEEE Trans. Ultrason., Ferroelectr., Freq. Control*, vol. 68, no. 5, pp. 1496–1510, May 2021.

[45] P. B. Rosnitskiy, B. A. Vysokanov, L. R. Gavrilov, O. A. Sapozhnikov, and V. A. Khokhlova, "Method for designing multielement fully populated random phased arrays for ultrasound surgery applications," *IEEE Trans. Ultrason., Ferroelectr., Freq. Control*, vol. 65, no. 4, pp. 630–637, Apr. 2018.

[46] P. Ramaekers, M. de Greef, R. Berriet, C. T. W. Moonen, and M. Ries, "Evaluation of a novel therapeutic focused ultrasound transducer based on Fermat's spiral," *Phys. Med. Biol.*, vol. 62, no. 12, pp. 5021–5045, Jun. 2017.

[47] O. Martínez-Graullera, C. J. Martín, G. Godoy, and L. G. Ullate, "2D array design based on Fermat spiral for ultrasound imaging," *Ultrasonics*, vol. 50, no. 2, pp. 280–289, Feb. 2010.

[48] A. Ramalli, E. Boni, A. S. Savoia, and P. Tortoli, "Density-tapered spiral arrays for ultrasound 3-D imaging," *IEEE Trans. Ultrason., Ferroelectr., Freq. Control*, vol. 62, no. 8, pp. 1580–1588, Aug. 2015.

[49] A. Ramalli et al., "High-frame-rate tri-plane echocardiography with spiral arrays: From simulation to real-time implementation," *IEEE Trans. Ultrason., Ferroelectr., Freq. Control*, vol. 67, no. 1, pp. 57–69, Jan. 2020.

[50] A. Ramalli et al., "Real-time 3-D spectral Doppler analysis with a sparse spiral array," *IEEE Trans. Ultrason., Ferroelectr., Freq. Control*, vol. 68, no. 5, pp. 1742–1751, May 2021.

[51] S. Harput et al., "3-D super-resolution ultrasound imaging with a 2-D sparse array," *IEEE Trans. Ultrason., Ferroelectr., Freq. Control*, vol. 67, no. 2, pp. 269–277, Feb. 2020.

[52] L. Wei et al., "High frame rate volumetric imaging of microbubbles using a sparse array and spatial coherence beamforming," *IEEE Trans. Ultrason., Ferroelectr., Freq. Control*, vol. 68, no. 10, pp. 3069–3081, Oct. 2021.

[53] R. Maffett et al., "Unfocused field analysis of a density-tapered spiral array for high-volume-rate 3-D ultrasound imaging," *IEEE Trans. Ultrason., Ferroelectr., Freq. Control*, vol. 69, no. 10, pp. 2810–2822, Oct. 2022.

[54] S. Nooijens, A. Ramalli, M. Ingram, M. Fournelle, A. Bertrand, and J. D'hooge, "Design of a sparse ellipsoidal array for volumetric ultrasound imaging of the prostate," in *Proc. IEEE Int. Ultrason. Symp.*, Sep. 2020, pp. 1–3.

[55] X. Li, A. Gachagan, and P. Murray, "Design of 2D sparse array transducers for anomaly detection in medical phantoms," *Sensors*, vol. 20, no. 18, p. 5370, Sep. 2020.

[56] H. Yoon and T.-K. Song, "Sparse rectangular and spiral array designs for 3D medical ultrasound imaging," *Sensors*, vol. 20, no. 1, p. 173, Dec. 2019.

[57] T. L. Szabo, *Diagnostic Ultrasound Imaging: Inside Out*, 2nd ed. Amsterdam, The Netherlands: Elsevier, 2014.

[58] A. Stuart Savoia et al., "A 256-element spiral CMUT array with integrated analog front end and transmit beamforming circuits," in *Proc. IEEE Int. Ultrason. Symp. (IUS)*, Oct. 2018, pp. 206–212.

[59] H. J. Vos et al., "Sparse volumetric PZT array with density tapering," in *Proc. IEEE Int. Ultrason. Symp. (IUS)*, Oct. 2018, pp. 1–4.

[60] L. Wei et al., "Sparse 2-D PZT-on-PCB arrays with density tapering," *IEEE Trans. Ultrason., Ferroelectr., Freq. Control*, vol. 69, no. 10, pp. 2798–2809, Oct. 2022.

[61] E. Sarradj, "A generic approach to synthesize optimal array microphone arrangements," in *Proc. 6th Berlin Beamforming Conf.*, 2016, pp. 1–12.

[62] H. L. Van Trees, *Optimum Array Processing: Part IV of Detection, Estimation, and Modulation Theory*. Hoboken, NJ, USA: Wiley, 2004.

[63] S. Bae, J. Park, and T.-K. Song, "Contrast and volume rate enhancement of 3-D ultrasound imaging using aperiodic plane wave angles: A simulation study," *IEEE Trans. Ultrason., Ferroelectr., Freq. Control*, vol. 66, no. 11, pp. 1731–1748, Nov. 2019.

[64] S. F. Liew, H. Noh, J. Trevino, L. D. Negro, and H. Cao, "Localized photonic band edge modes and orbital angular momenta of light in a golden-angle spiral," *Opt. Exp.*, vol. 19, no. 24, p. 23631, 2011.

[65] G. Allevato et al., "Real-time 3-D imaging using an air-coupled ultrasonic phased-array," *IEEE Trans. Ultrason., Ferroelectr., Freq. Control*, vol. 68, no. 3, pp. 796–806, Mar. 2021.

GIANNI ALLEVATO received the M.Sc. degree in electrical engineering from Technische Universtität Darmstadt (TU Darmstadt), Germany, in 2018. Since 2018, he has been a Research Associate with the Measurement and Sensor Technology Group, TU Darmstadt. His research interests include electronics and embedded system design, array design, software development, and parallel signal processing for imaging with air-coupled ultrasonic phased arrays and its applications.

CHRISTOPH HAUGWITZ (Student Member, IEEE) received the M.Sc. degree in electrical engineering from Technische Universität Darmstadt (TU Darmstadt), Germany, in 2021. Since then, he has been a Research Associate with the Measurement and Sensor Technology Group, TU Darmstadt. His research interests include ultrasonic flow metering and air-coupled ultrasonic phased arrays and its applications.

MATTHIAS RUTSCH received the B.Sc. degree from Brandenburgische Technische Universität Cottbus-Senftenberg, Germany, in 2014, and the M.Sc. degree in electrical engineering from Technische Universität Darmstadt (TU Darmstadt), Germany, in 2017. Since then, he has been a Research Associate with the Measurement and Sensor Technology Group, TU Darmstadt. His research interests include simulation and characterization of duct acoustics for air-coupled ultrasound applications.

RAPHAEL MÜLLER received the M.Sc. degree in electrical engineering and information technology from Technische Universität Darmstadt (TU Darmstadt), Darmstadt, Germany, in 2020. Since then, he has been a Research Associate with the Communication Systems Group, TU Darmstadt. His research interests include multilinear algebra and sensor array processing, especially sparse signal processing and its application to radar and ultrasound imaging.

MARIUS PESAVENTO (Senior Member, IEEE) received the Dipl-Ing. degree from Ruhr-Universität Bochum, Bochum, Germany, in 1999, the M.Eng. degree from McMaster University, Hamilton, ON, Canada, in 2000, and the Dr.-Ing. degree in electrical engineering from Ruhr-Universität Bochum in 2005. From 2005 to 2009, he was a Research Engineer with two startup companies. He was also an Assistant Professor of robust signal processing and a Full Professor of communication systems with the Department of Electrical Engineering and Information Technology, Technische Universität Darmstadt, Darmstadt, Germany, in 2010 and 2013, respectively. His research interests include robust signal processing and adaptive beamforming, high-resolution sensor array processing, multiantenna and multiuser communication systems, distributed, sparse, and mixed-integer optimization techniques for signal processing and communications, statistical signal processing, spectral analysis, and parameter estimation.

MARIO KUPNIK (Senior Member, IEEE) received the Dipl.-Ing. degree in electrical engineering from the Graz University of Technology, Austria, in 2000, and the Ph.D. degree in electrical engineering from the University of Leoben, Leoben, Austria, in 2004. From 2005 to 2011, he was a Post-Doctoral Researcher, a Research Associate, and a Senior Research Scientist with the Edward L. Ginzton Laboratory, Stanford University, Stanford, CA, USA. From 2011 to 2014, he was a Full Professor of electrical engineering with the Brandenburg University of Technology, Cottbus, Germany. Since 2015, he has been a Full Professor with the Technische Universität Darmstadt, Germany, where he is currently the Head of the Measurement and Sensor Technology Group. His research interests include micromachined sensors and actuators, multiphysics simulations, ferroelectrets, flowmetering of gases and liquids, ultrasound, electroacoustics, human–machine interaction, and robotics.

• • •